

OBSERVATIONAL SIGNATURES OF MASS-LOADING IN JETS LAUNCHED BY ROTATING BLACK HOLES

MICHAEL O' RIORDAN^{1*}, ASAF PE'ER¹, AND JONATHAN C. MCKINNEY²

¹Physics Department, University College Cork, Cork, Ireland

²Department of Physics and Joint Space-Science Institute, University of Maryland, College Park, MD 20742, USA

ABSTRACT

It is widely believed that relativistic jets in X-ray binaries and active-galactic nuclei are powered by the rotational energy of black holes. This idea is supported by general-relativistic magnetohydrodynamic (GRMHD) simulations of accreting black holes, which demonstrate efficient energy extraction via the Blandford-Znajek mechanism. However, due to uncertainties in the physics of mass-loading, and the failure of GRMHD numerical schemes in the highly-magnetized funnel region, the matter content of the jet remains poorly constrained. We investigate the observational signatures of mass-loading in the funnel by performing general-relativistic radiative transfer calculations on a range of 3D GRMHD simulations of accreting black holes. We find significant observational differences between cases in which the funnel is empty and cases where the funnel is filled with plasma, particularly in the optical and X-ray bands. In the context of Sgr A*, current spectral data constrains the jet filling only if the black hole is rapidly rotating with $a \gtrsim 0.9$. In this case, the limits on the infrared flux disfavour a strong contribution from material in the funnel. We comment on the implications of our models for interpreting future Event Horizon Telescope observations. We also scale our models to stellar-mass black holes, and discuss their applicability to the low-luminosity state in X-ray binaries.

1. INTRODUCTION

Relativistic jets are a ubiquitous phenomenon. They have been observed across a range of accreting black hole systems spanning more than 8 orders of magnitude in mass – from stellar-mass black holes in X-ray binaries (XRBs), to supermassive black holes in active galaxies. The Blandford-Znajek (BZ) process (Blandford & Znajek 1977), in which rotational energy is extracted electromagnetically from a Kerr black hole, is widely regarded as a plausible mechanism for driving these jets. In a force-free black hole magnetosphere, the BZ model predicts that energy is extracted from the black hole at a rate $P_{\text{BZ}} = \kappa \Phi^2 \Omega_H^2 / 4\pi c$ (Blandford & Znajek 1977; Tchekhovskoy et al. 2010). Here, κ is a dimensionless number which depends on the magnetic field geometry, Φ is the magnetic flux threading the horizon, $\Omega_H = ac/2r_H$ is the angular velocity of the horizon, a is the dimensionless black hole spin, $r_H = (1 + \sqrt{1 - a^2}) r_g$ is the horizon radius, and $r_g = GM/c^2$ is the gravitational radius. The expected BZ jet power therefore depends strongly on the black hole spin, as well as the properties of the near-horizon magnetic field.

Sophisticated, global general-relativistic magnetohydrodynamic (GRMHD) simulations have largely con-

firmed the basic predictions of the BZ model. In particular, Tchekhovskoy et al. (2011) and McKinney et al. (2012) demonstrated jet-launching with efficiencies exceeding 100%, meaning that more energy flows out of the black hole than flows in. Such high efficiencies are only possible if enough ordered vertical magnetic flux can accumulate near the horizon. In this case, the magnetic pressure becomes comparable to the gas pressure, disrupting the inner accretion flow and forming a “magnetically arrested disk” (MAD; Narayan et al. 2003). By contrast, non-MAD flows (called SANE by Narayan et al. 2012) typically do not show very efficient energy extraction, even at high black hole spin, due to the turbulent, disordered fields at the horizon (McKinney & Blandford 2009).

In recent years, MAD and SANE GRMHD models have been used extensively to model Sgr A*, the extremely low-luminosity accreting supermassive black hole at the centre of our Galaxy (Mościbrodzka et al. 2009; Shcherbakov et al. 2012; Mościbrodzka & Falcke 2013; Mościbrodzka et al. 2014; Chan et al. 2015b,a; Ball et al. 2016; Ressler et al. 2017; Gold et al. 2017). These studies have largely been motivated by very-long baseline interferometric (VLBI) observations with the Event Horizon Telescope (EHT; Doeleman et al. 2009a), which will soon resolve structure in Sgr A* on spatial scales comparable to the Schwarzschild radius. The EHT will

*michael_oriordan@umail.ucc.ie

also resolve small-scale polarized structure, which carries information about the near-horizon magnetic field. Therefore, the EHT offers an unprecedented opportunity to test theories of accretion and jet-launching, and possibly even general relativity itself via measurements of the black hole shadow (e.g., [Psaltis et al. 2015](#), and references therein).

Despite these important advances, significant theoretical uncertainties remain which hinder a direct comparison between the dynamical models and observations. In particular, there is considerable uncertainty in the mass-loading physics of BZ jets. It is well known that GRMHD codes fail inside the highly-magnetized funnel ([Gammie et al. 2003](#)). In particular, numerical errors accumulate when the ratio of the magnetic energy density to mass energy density becomes large. In what follows, we will refer to this ratio as the magnetization σ . To keep the numerical scheme stable, GRMHD codes typically inject matter when σ becomes larger than some (rather arbitrary) value. This effectively enforces a minimum density in the simulation, commonly referred to as a density floor. Although there are physical processes which may operate to mass-load the funnel, for example pair cascades ([Blandford & Znajek 1977](#); [Levinson & Rieger 2011](#); [Broderick & Tchekhovskoy 2015](#)) or photon annihilation ([Mościbrodzka et al. 2011](#)), the injection of floor material is arbitrary and chosen simply to avoid numerical issues. Therefore, the funnel mass and internal energy densities are not determined by the GRMHD simulations.

Although the injected floor material has little effect on the dynamics, it can affect the resulting spectra and so must be considered when comparing GRMHD models with observations. Depending on the choice of initialisation for the floors, the plasma in the funnel might be tenuous enough such that it has a negligible contribution to the spectra. In this case, the jet emission is dominated by the funnel wall or “jet sheath” as in [Mościbrodzka & Falcke \(2013\)](#) and [Mościbrodzka et al. \(2014\)](#). This “empty funnel” situation can also be achieved by simply removing floor material from the funnel during the radiative transport calculation. The material to remove can be chosen in a number of ways, for example as cells in a large bipolar cone ([Shcherbakov & McKinney 2013](#)), cells considered artificially hot or dense relative to their neighbours ([Chan et al. 2015b](#)), or cells with a large value of σ ([O' Riordan et al. 2016a,b](#)).

Recently, [Gold et al. \(2017\)](#) argued that the prescription used for treating the funnel material could be very important when interpreting future observations from the EHT. In particular, they showed that the black hole shadow can be completely obscured in the case of significant emission from the funnel, while the absence of strong funnel emission can in fact mimic features of the

shadow. Therefore, in order to test general relativity using EHT observations it will be crucial to distinguish between features caused by strong-field gravity and those arising from the presence or absence of emitting matter in the jet.

In this work, we investigate the observational effects of mass-loading in the regime where the funnel remains force-free. That is, we restrict our analysis to the case where the funnel material is highly-magnetized with $\sigma \gtrsim 10$. In the opposite regime where the inertia of the funnel plasma cannot be neglected ($\sigma \lesssim 1$), [Globus & Levinson \(2013\)](#) showed that mass and energy loading of the field lines can strongly suppress or even switch off energy extraction from the black hole. This case would therefore involve significant modifications to the dynamical GRMHD models. We will study the observational consequences of this regime in a future work.

The structure of the paper is as follows. In [Section 2](#) we briefly describe our GRMHD models, radiative transport code, and prescriptions for treating the electrons in the jet. In [Section 3](#) we show the spectra from our GRMHD models and describe the observational effects of mass-loading the funnel. In [Section 4](#) we summarise and discuss our findings. Throughout the paper we use units where $G = c = 1$, which implies that the gravitational radius r_g and light-crossing time $t_g = r_g/c$ become $r_g = t_g = M$. We will occasionally reintroduce factors of c for clarity.

2. MODELS

We consider six MAD accretion flows from [Tchekhovskoy et al. \(2011\)](#) and [McKinney et al. \(2012\)](#), and a SANE accretion flow from [McKinney & Blandford \(2009\)](#). Five of our MAD models have a scale height of $H/R \approx 0.2$ and spins of $a = \{0.1, 0.2, 0.5, 0.9, 0.99\}$. These are called A0.1N100, A0.2N100, A0.5N100, A0.9N100, and A0.99N100 in [McKinney et al. \(2012\)](#). We will refer to these as our “thin MAD” models. We also consider a very geometrically-thick MAD model with $H/R \approx 1$ and a spin of $a = 0.9375$, called A0.94BfN40 in [McKinney et al. \(2012\)](#). We will refer to this model as “thick MAD”. Finally, we consider a SANE model with $H/R \approx 0.2$ and a spin of $a = 0.92$, called MB09D in [McKinney et al. \(2012\)](#).

In [Figure 1](#) we show snapshots of our MAD and SANE models. The colour shows the mass density and the black contours show the structure of the poloidal magnetic field (from the ϕ -integrated vector potential). The top panel shows the thin MAD model with $a = 0.99$, the middle panel shows the thick MAD model with $a = 0.9375$, and the bottom panel shows the SANE model with $a = 0.92$. The MAD models have large-scale, ordered poloidal fields in the disk and jet, while the disk in the SANE model has a more disordered field. In all

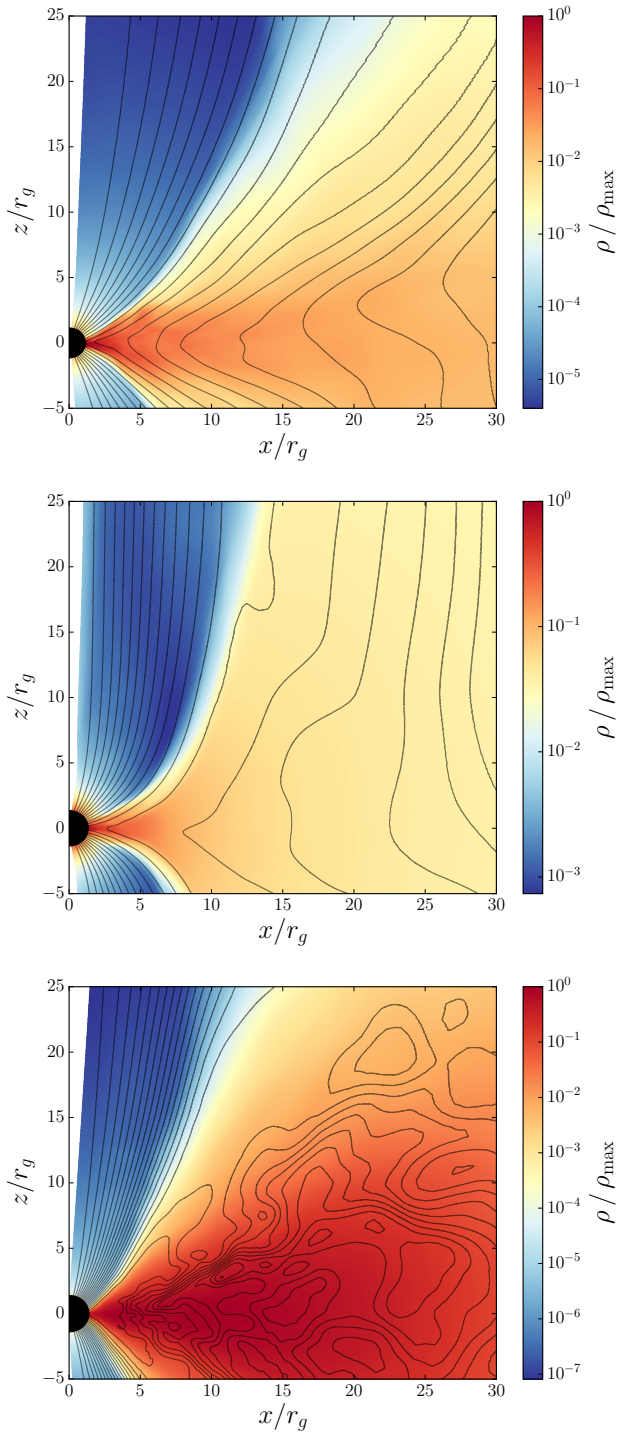


Figure 1. Snapshots of our MAD and SANE GRMHD models. The colour shows the mass density and the poloidal magnetic field lines are represented by the black contours. The top panel shows the thin MAD model with $H/R \approx 0.2$ and $a = 0.99$. The middle panel shows the thick MAD model with $H/R \approx 1$ and $a = 0.9375$. The bottom panel shows the SANE model with $H/R \approx 0.2$ and $a = 0.92$. Both MAD models have large-scale ordered poloidal fields in the disk and jet.

models, we remove material from cells near the poles as coordinate singularities can cause numerical issues here. This is indicated as an excised region along the z -axis in Figure 1. Detailed descriptions of these models can be found in McKinney & Blandford (2009); Tekehovskoy et al. (2011); McKinney et al. (2012); O’ Riordan et al. (2016a,b).

We calculate the spectra from these models using a general-relativistic radiative transport code based on `grmonty` (Dolence et al. 2009). We use snapshots from the GRMHD simulations as input, and include contributions to the spectra from synchrotron emission, absorption, and Compton scattering from relativistic thermal electrons. The mass accretion rates in our low-luminosity target applications of Sgr A* and the low/hard state in XRBs are expected to be well below the corresponding Eddington rate, which justifies treating the radiation in a post-processing step. The Eddington rate is defined as $\dot{M}_{\text{Edd}} c^2 \equiv 10 L_{\text{Edd}} \approx 10^{39} \left(\frac{M}{M_{\odot}}\right) \text{erg s}^{-1}$ (Narayan & McClintock 2008). Since differences in mass density and magnetization can cause different heating and cooling rates for the protons and electrons in the disk and jet (e.g., Ressler et al. 2015; Foucart et al. 2016), we specify the proton-to-electron temperature ratio $\mathcal{T} \equiv T_p/T_e$ as a function of the plasma $\beta \equiv p_{\text{gas}}/p_{\text{mag}}$. Here, p_{gas} is the thermal pressure of the fluid, and p_{mag} is the magnetic pressure. In order to maximize the potential contributions from the highly-magnetized funnel material, unless otherwise specified, we choose a critical value of $\beta_c = 0.2$ and set $\mathcal{T} = \mathcal{T}_{\text{disk}} = 30$ in regions where $\beta > \beta_c$, and $\mathcal{T} = \mathcal{T}_{\text{jet}} = 3$ in regions where $\beta \leq \beta_c$. For simplicity, we will refer to regions with $\beta \leq \beta_c$ as the “jet”, and regions with $\beta > \beta_c$ as the “disk”. In particular, the “jet” includes both the funnel wall and central funnel matter. Although the choice of β_c is somewhat arbitrary, we find that using $\beta_c = 0.2$ gives a reasonable distinction between the disk and jet, and our results are largely unaffected by small changes in β_c up to a factor of a few. We impose a smooth, exponential transition between the temperature ratios in the disk and jet by setting $\mathcal{T} = \mathcal{T}_{\text{jet}} e^{-\beta/\beta_c} + \mathcal{T}_{\text{disk}} (1 - e^{-\beta/\beta_c})$.

To maintain numerical stability, GRMHD codes must inject material into the low-density, highly-magnetized, funnel region. In particular, numerical errors accumulate when the magnetization becomes large $\sigma = b^2/\rho \gg 1$. Here, $b^2 = b^\mu b_\mu$, b^μ is the magnetic four-field, and ρ is the rest-mass density. The magnetic four-field can be written in terms of the lab-frame 3-field B^i as $b^\mu = h_\nu^\mu B^\nu/u^t$, where u^μ is the fluid four-velocity and $h_\nu^\mu = \delta_\nu^\mu + u^\mu u_\nu$ is a projection tensor. In our units, the magnetic pressure is related to the magnetization by $p_{\text{mag}} = \sigma\rho/2$. Although the injected numerical den-

sity floors do not affect the dynamics, they can be artificially hot and so might affect the resulting spectra. In O' Riordan et al. (2016a,b), we considered the case where the material from the centre of the funnel doesn't contribute significantly to the observed spectrum. That is, we removed the floor material such that the middle of the funnel region was empty. In this work, we follow the same procedure for removing the floor material and will refer to the resulting models as “empty”. For removing the floors, we set the density to zero in regions where $\sigma > \sigma_c(r)$. We use $\sigma_c = 20$ at the horizon, and linearly interpolate to $\sigma_c = 10$ at $r = 10r_g$. For larger radii, we use a fixed value of $\sigma_c = 10$. This ensures that the injected floors are removed, without removing material close to the black hole which naturally becomes highly magnetized. Using this prescription, the centre of the funnel region is removed while the disk and funnel wall are not affected.

We also consider the case where the funnel is mass-loaded and will refer to these models as “filled”. When modelling the filled funnel, we restrict our attention to the regime in which the mass-loading of the jet doesn't affect the magnetic field in the funnel. In covariant form, the energy and momentum exchange between an electromagnetic field and charged matter can be written as $\nabla_\mu T_{EM}^{\mu\nu} = -F^{\mu\nu} j_\nu$, where ∇_μ is the covariant derivative, $T_{EM}^{\mu\nu} = F^{\mu\alpha} F^\nu{}_\alpha - \frac{1}{4} g^{\mu\nu} F_{\alpha\beta} F^{\alpha\beta}$ is the electromagnetic stress-energy tensor, $F^{\mu\nu}$ is the electromagnetic field tensor, j^μ is the electric four-current density, and $g_{\mu\nu}$ is the metric. In the case where the plasma energy-momentum is many orders of magnitude less than that of the electromagnetic field, the energy and momentum exchange can be neglected. In this case, the electromagnetic stress-energy tensor is conserved by itself $\nabla_\mu T_{EM}^{\mu\nu} = 0$. Such a situation is referred to as force-free because of the vanishing of the Lorentz four-force density $f^\mu = F^{\mu\nu} j_\nu$. The approximately force-free solution in the funnel will be preserved as long as the injected matter has $\sigma \gg 1$ (McKinney & Gammie 2004). In this regime we can treat the funnel mass-loading in a post-processing step. More significant mass-loading with $\sigma \lesssim 1$ would affect the fluid dynamics and could even quench the BZ jet (Globus & Levinson 2013). In the case of a strongly mass-loaded funnel, the resulting GRMHD solution may deviate significantly from the models described here.

For our filled models, we first remove the floor material using the procedure described above, and fill the empty funnel cells at each radius with constant mass and internal energy densities, equal to their corresponding values at the edge of the funnel wall. We then re-scale the material in the funnel and funnel wall to conserve energy. In practise, this re-scaling has little effect on the resulting spectra. Using this procedure, the proper-

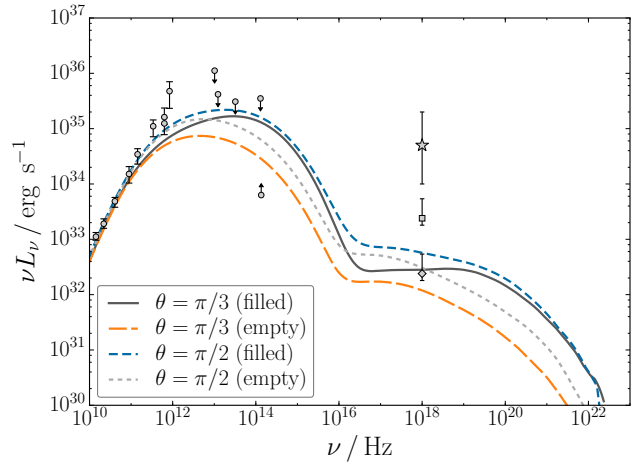


Figure 2. Comparison of the spectra for the empty and filled funnel thin MAD models with $a = 0.1$. The radio data points and IR limits are the same as those considered by Chan et al. (2015b). The X-ray flux during quiescence is marked by the square data point (Baganoff et al. 2003), while the diamond marks 10% of the quiescent X-ray flux (Neilsen et al. 2013). The range of observed X-ray flares is represented by the star Neilsen et al. (2013). The radio emission originates in the funnel wall and so is not sensitive to the mass-loading of the funnel. The funnel material primarily contributes to the IR and optical bands, with a corresponding increase in the synchrotron self-Compton component. In this low-spin case, both the empty and filled funnel models are largely consistent with the data.

ties of the plasma in the funnel are determined by the self-consistent material in the funnel wall. The resulting matter distribution in the funnel is in fact similar to the original floor material shown in Figure 1. However, we choose to manually fill the funnel to avoid any potential issues with artificially hot cells, which would otherwise have to be checked and removed as in Chan et al. (2015b). We show the mass and internal energy density distributions in our empty and filled models in Figure A1.

3. RESULTS

3.1. Predictions for spectra of Sgr A*

To scale our GRMHD models to Sgr A*, we set the black hole mass to be $M = 4 \times 10^6 M_\odot$ (Gillessen et al. 2009) and adjust the mass accretion rate so that the resulting flux at 230 GHz is roughly consistent with the observational data. This emission likely originates from within a few Schwarzschild radii of the supermassive black hole (Doeleman et al. 2008), a region which is well resolved by the GRMHD simulations and has reached a quasi-steady state. In Figure 2 we show spectra from the thin MAD model with a black hole spin of $a = 0.1$, for two different observer inclinations of $\theta = \pi/2$ (perpendicular to the spin axis), and $\theta = \pi/3$. The “empty” model corresponds to the case where the funnel material does not contribute significantly to the observed spec-

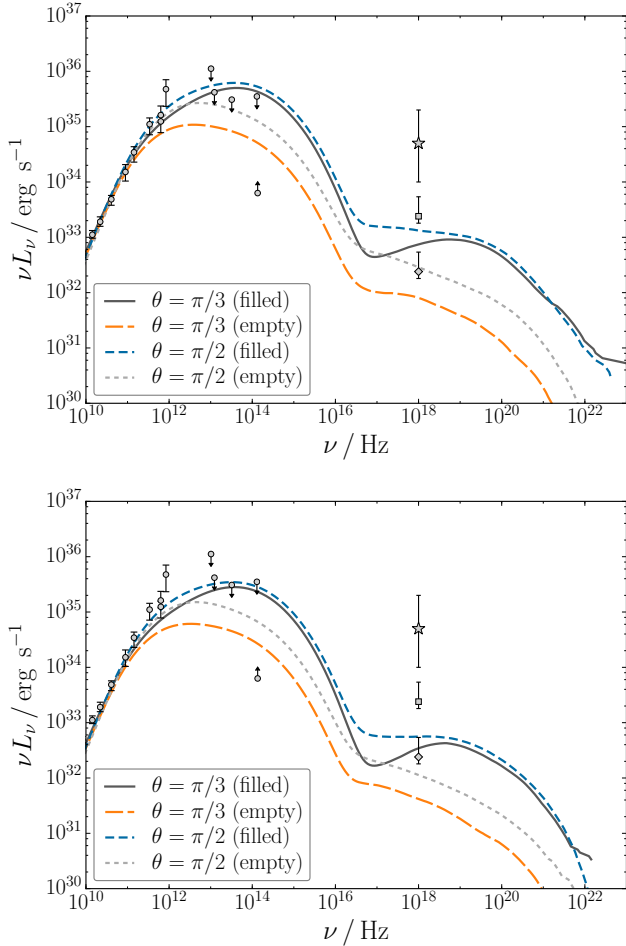


Figure 3. Spectra for the thin MAD model with $a = 0.5$. The spectra are qualitatively similar to the $a = 0.1$ case, but with a larger contribution from the funnel material. To obtain better fits with the filled model, the accretion rate in the bottom panel has been decreased by a factor of ~ 1.5 relative to that in the top panel. Although both the empty and filled funnel models are consistent with the data, the IR emission in the filled funnel case is close to the maximum flux allowed by observations.

tra. In this case, we have removed all the plasma from the centre of the funnel and so the emission originates in the accretion disk and in the funnel wall. The “filled” model corresponds to the extreme case where the funnel is filled with constant profiles of mass and internal energy densities. The values are chosen to be equal to those at the edge of the funnel wall.

The radio data points and IR limits are the same as those considered by Chan et al. (2015b). In particular, the IR limits represent the highest and lowest observed fluxes. The X-ray flux during quiescence is marked by the square data point (Baganoff et al. 2003). The diamond marks 10% of the quiescent X-ray flux, which is the estimated contribution from the inner accretion flow (Neilsen et al. 2013). The range of observed X-ray flares is represented by the star and corresponding error bars

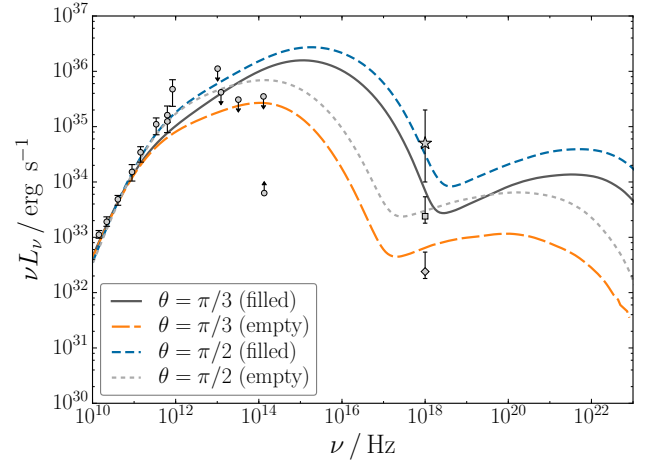


Figure 4. Spectra for the thin MAD model with $a = 0.9$. In this case the IR limits and X-ray estimates disfavour a filled funnel component. Even the empty funnel case is approaching the limits of the observations. While a lower accretion rate would decrease the IR and X-ray flux towards values more consistent with the data, the radio flux would then be missed by a large amount.

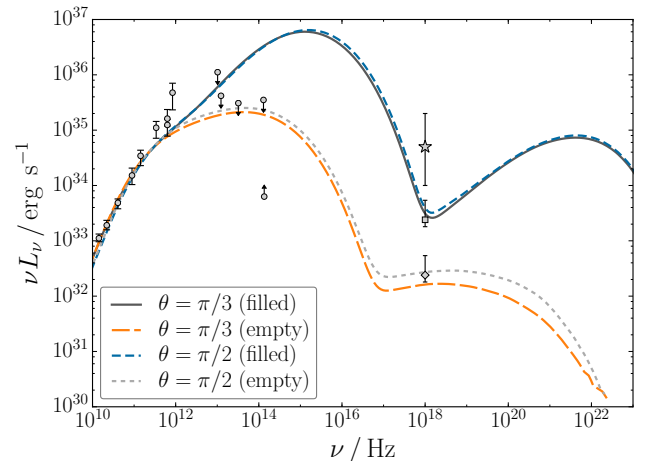


Figure 5. Spectra for the thin MAD model with $a = 0.99$. As with the $a = 0.9$ case, the IR and X-ray data disfavour the filled funnel model. Furthermore, fitting the empty funnel model to the data requires suppressing the emission from close to the horizon by increasing the proton-to-electron temperature ratio of the inflowing material.

Neilsen et al. (2013).

The mass accretion rate in Figure 2 is set such that the average rate at the horizon is $\dot{M} \approx 10^{-7} \dot{M}_{\text{Edd}}$. Interestingly, the radio emission at frequencies $\nu \lesssim 10^{12}$ Hz is not sensitive to the mass-loading of the funnel. This is because this emission is dominated by the funnel wall. This is consistent with the findings of Mościbrodzka et al. (2014), who refer to this region as the “jet sheath”. Although there is a clear increase at IR and optical frequencies relative to the empty funnel case, both the empty and filled funnel models are largely consistent

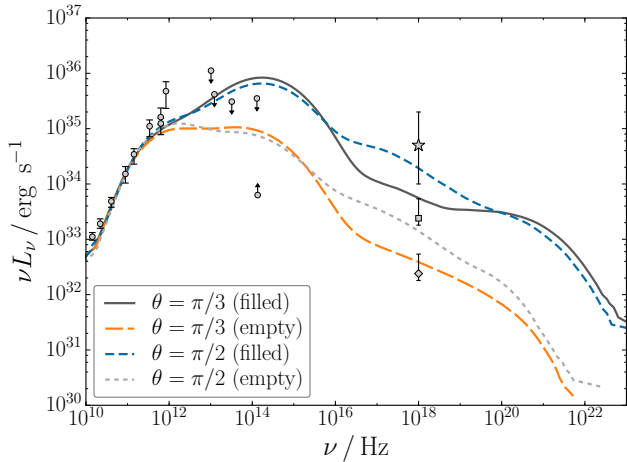


Figure 6. Spectra for the SANE model with $a = 0.92$. As in the high-spin MAD models, the IR limits disfavour models with strong funnel emission.

with the data.

In Figure 3 we show the spectra for the higher-spin case of $a = 0.5$. The spectra are qualitatively similar to those in Figure 2, however the enhancement at IR and optical frequencies is larger. To obtain better fits with the filled model, we reduced the accretion rate by a factor of ~ 1.5 in the bottom panel relative to the top panel. The increase in this synchrotron self-Compton emission in the hard X-rays. As with the $a = 0.1$ model, both the empty and filled funnel cases fit the data reasonably well, however, the IR flux in the filled model is very close to the upper limits on the observed flux.

In Figure 4 we show the thin MAD model with $a = 0.9$. The IR and X-ray limits clearly disfavour the case where the funnel material contributes significantly to the emission. Although the X-ray and IR emission can be brought within the limits by adjusting the mass accretion rate, this would also significantly reduce the radio flux which originates in the funnel wall and which is independent of the mass-loading. The difference between the empty and filled models is even more dramatic in the extreme $a = 0.99$ case, which we show in Figure 5. As discussed in O' Riordan et al. (2016a), the emission from this model is strongly dominated by the near-horizon plasma. In order to give reasonable fits to the data, even in the empty funnel case, we suppressed this near-horizon radiation by imposing a temperature ratio of $\mathcal{T} = 300$ on the inflowing material. A similar result was found by Chan et al. (2015b), whose best-fit MAD models have very large proton-to-electron temperature ratios in the disk.

In Figure 6 we show the spectra calculated from our SANE model with $a = 0.92$ and a mass accretion rate of

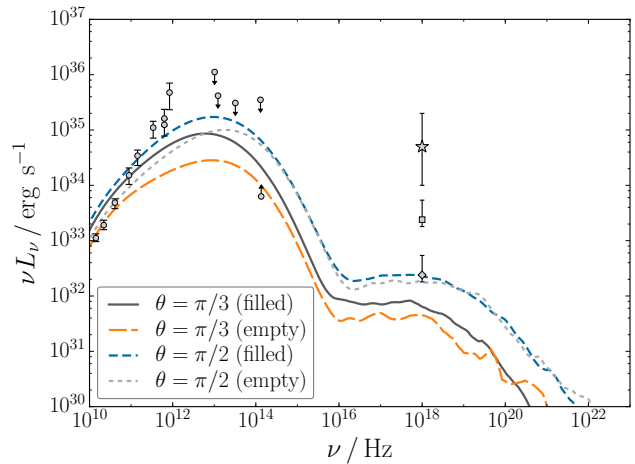
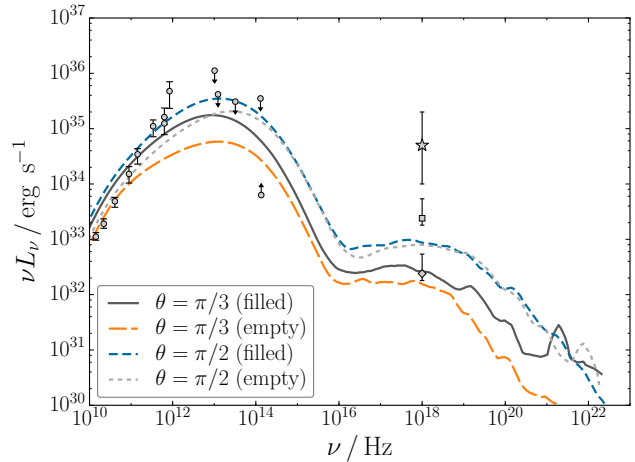


Figure 7. Spectra for the geometrically-thick ($H/R \approx 1$) MAD model with $a = 0.9375$. The accretion rate in the top panel is larger than that in the bottom panel by a factor of ~ 1.5 . This model gives a poorer fit to the radio data than the geometrically thinner models. In this case, although the black hole is rotating rapidly, both the empty and filled models provide reasonably similar fits to the data. This is because the funnel emission is somewhat suppressed relative to the other models and so the difference between empty and filled funnels is less extreme.

$\dot{M} \approx 10^{-6} \dot{M}_{\text{Edd}}$. This model has the same scale height of $H/R \approx 0.2$ as our thin MAD models. As in the thin MAD case, the radio emission is insensitive to the mass loading of the funnel. The higher mass accretion rate results in a larger optical depth, which is clearly reflected in the high-energy parts of the spectra that show multiple Compton scatterings. Interestingly, as in the high-spin MAD models, the filled funnel model significantly over-produces IR emission and so an empty funnel is favoured by the data.

To conclude, for all our thin MAD models and our SANE model, we find that the radio flux is dominated by the funnel wall and is largely independent of the mass-loading of the jet. We also find a significantly larger IR flux in the filled models than in the empty models.

From this, we expect that the ratio of the IR flux and 230 GHz flux could be used as a probe of mass-loading processes in the funnel. Furthermore, in the context of Sgr A*, although our low-spin models are consistent with the data in both empty and filled funnel cases, the higher-spin models only fit the data provided the funnel material does not contribute significantly to the observed spectrum.

In Figure 7 we show the spectra calculated from our thick MAD model which has a black hole spin of $a = 0.9375$ and a very geometrically-thick disk ($H/R \approx 1$). As in Figure 3, the accretion rate in the bottom panel is ~ 1.5 times lower than that in the top panel. Although the emission from our thin MAD and SANE models is dominated by the region $r \lesssim 30M$, which has reached a quasi-steady state, the outer radii of our thick MAD model can contribute significantly to the emission. The outer radii of our GRMHD models have not had enough time to reach a steady state and so the plasma properties depend strongly on the initial conditions in the torus. Furthermore, the 230 GHz flux which we have been using to normalise our models likely originates in the inner few r_g of the accretion flow (Doeleman et al. 2008). Therefore, we follow the procedure of Shcherbakov et al. (2012) to analytically extend the fluid quantities to large radii. We extend the fluid properties at $r = 30M$ as power-laws out to the Bondi radius in order to match the estimated density and temperature for Sgr A* at this radius. We further assume an isothermal jet with electron temperature $\Theta = kT/mc^2 = 50$ (Mościbrodzka et al. 2014; Chan et al. 2015b; Gold et al. 2017), which provides a better fit to the radio emission than a constant temperature ratio for this model. The difference between the empty and filled funnel models is smaller than in the high-spin thin MAD and SANE cases and so both provide similar fits to the data. Contrary to the previous cases, the funnel filling primarily affects the lower-frequency emission. This is consistent with Gold et al. (2017), who found that the 230 GHz images of their models were affected by the funnel filling. We will perform a more thorough investigation of the dependence on the disk scale height and prescriptions for extending the data to the Bondi radius in a future work.

3.2. Predictions for spectra of the low/hard state in XRBs

In this section we scale our thin MAD models to the low luminosity state in XRBs by setting the black hole mass to $M = 10M_\odot$. For comparing the different GRMHD models, we fix the mass accretion rate to be $\dot{M} \approx 10^{-6} \dot{M}_{\text{Edd}}$. To maximize the potential effects of the funnel emission, we again consider the case where the proton-to-electron temperature ratios in the disk and jet are $\mathcal{T}_{\text{disk}} = 30$ and $\mathcal{T}_{\text{jet}} = 3$.

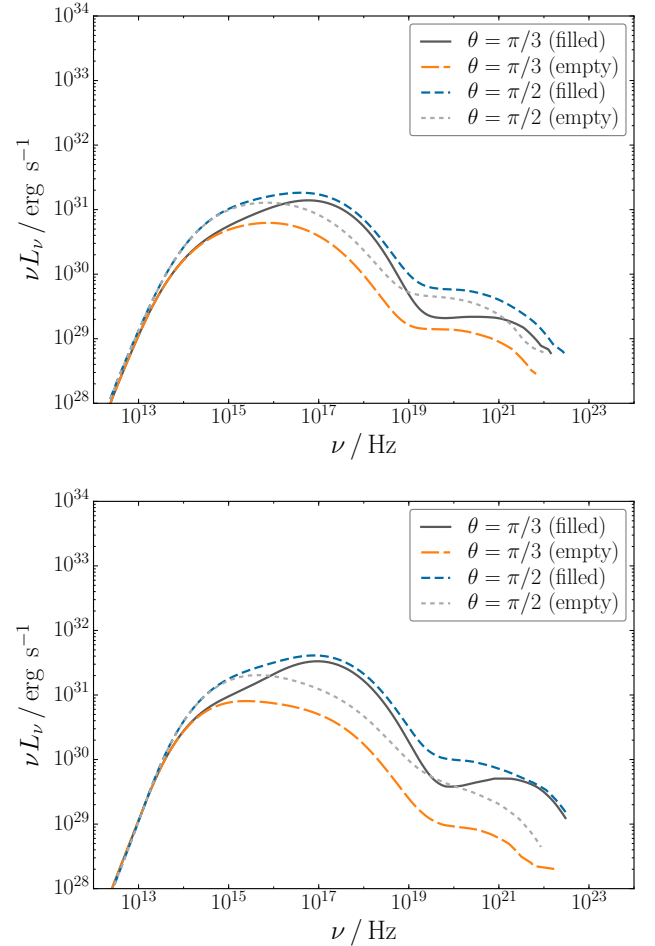


Figure 8. Spectra for thin MAD models with $a = 0.1$ (top), and $a = 0.5$ (bottom). The black hole mass has been set to $M = 10M_\odot$. The spectra are qualitatively similar to the results for Sgr A*. The optical and lower frequency emission is insensitive to the funnel material, while the hard UV and soft X-rays are significantly enhanced relative to the empty funnel case.

In Figure 8 we show the spectra for the low-spin models with $a = 0.1$ and $a = 0.5$. The results are qualitatively similar to the corresponding spectra for Sgr A*, with differences in the peak frequencies and overall luminosity due to changes in the black hole mass and accretion rate. In particular, we find that the filled funnel models show enhanced hard UV/soft X-ray emission, while the optical and lower-frequency fluxes are unaffected by the mass-loading.

In Figure 9 we show the spectra for the high-spin models with $a = 0.9$ and $a = 0.99$. We find very large differences between the empty and filled funnel models, with the funnel contribution shifting to higher frequencies. In this case, the X-rays and γ -rays are significantly modified by the funnel matter, while frequencies below $\sim 10^{16}$ Hz are unaffected by the funnel contribution. In the $a = 0.99$ case, the radiative efficiency is large, approaching values $\gtrsim 10\%$, especially in the filled funnel

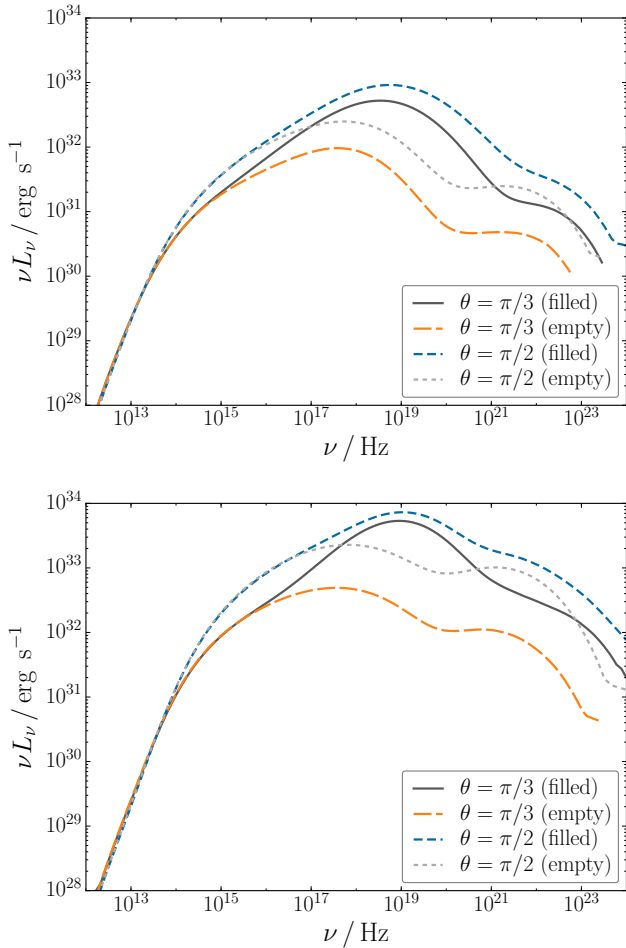


Figure 9. Spectra for the thin MAD models with $a = 0.9$ (top), and $a = 0.99$ (bottom). The X-ray flux is significantly higher in the filled funnel models, while emission at frequencies $\lesssim 10^{16}$ Hz is unaffected by the funnel matter.

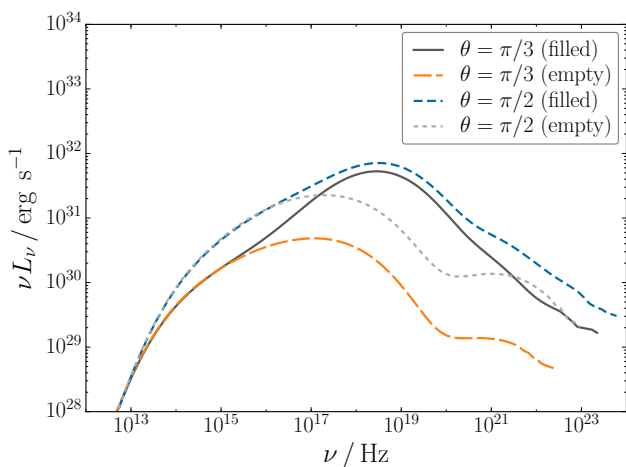


Figure 10. Same as the bottom panel of Figure 9, but with a lower accretion rate of $\dot{M} \approx 10^{-7} \dot{M}_{\text{Edd}}$. Although the luminosity is significantly lower than in the previous case, the frequencies at which the emission is enhanced are similar. This is due to the reasonably weak dependence of the frequency on the accretion rate.

model. A similar result was reported by [Ryan et al. \(2017\)](#), who found that accretion flows with $a = 0.5$ can approach 1% radiative efficiency by $\dot{M} \sim 10^{-5} \dot{M}_{\text{Edd}}$. To avoid complications due to radiative cooling, we investigate a lower accretion rate of $\dot{M} \approx 10^{-7} \dot{M}_{\text{Edd}}$, and show the resulting spectra in Figure 10. The spectra in the hard X-rays and below are qualitatively similar to those in Figure 9, and so our conclusions about the effects of the funnel mass-loading still hold. This is not surprising since, as shown in Appendix B, although the luminosity depends very strongly on the accretion rate $L_{\text{syn}} \sim \dot{M}^2$, the frequency depends only weakly on \dot{M} as $\nu_{\text{syn}} \sim \dot{M}^{1/2}$. There is a larger difference in the synchrotron self-Compton component due to the linear dependence of the Compton y parameter on \dot{M} (see Appendix B).

4. SUMMARY AND DISCUSSION

In this work, we investigated the observational effects of the mass-loading of BZ jets. As argued by [Gold et al. \(2017\)](#), understanding the mass-loading of the funnel will be extremely important for interpreting future EHT observations of the black hole shadow in Sgr A*. We considered the case in which the plasma in the funnel remains force-free, which allowed us to treat the mass-loading in a post-processing step. We found significant differences between models with an empty funnel and models where the funnel was filled with highly-magnetized plasma. In particular, in the context of Sgr A* the IR and optical flux is enhanced relative to the empty funnel case. Interestingly, the radio emission from our thin MAD and SANE models is dominated by the funnel wall and so is largely unaffected by the mass-loading. We therefore identify the ratio of the IR and 230 GHz flux as a potential observational probe of the filling factor of the funnel.

We find qualitatively similar results in the context of XRBs, although shifted to higher frequencies due to changes in the black hole mass and accretion rate. It is often argued that inverse Compton emission from a corona of hot electrons surrounding the inner accretion flow is responsible for the X-ray emission observed in XRBs (e.g., [Titarchuk 1994](#); [Magdziarz & Zdziarski 1995](#); [Gierlinski et al. 1997](#); [Esin et al. 1997, 2001](#); [Poutanen 1998](#); [Cadolle Bel et al. 2006](#); [Yuan et al. 2007](#); [Narayan & McClintock 2008](#); [Niedźwiecki et al. 2012, 2014](#); [Qiao & Liu 2015](#)). However, there is significant degeneracy between these models and ones in which a large fraction of the X-ray emission originates in the base of the jet (e.g., [Mirabel & Rodríguez 1994](#); [Markoff et al. 2001, 2003, 2005](#); [Falcke et al. 2004](#); [Bosch-Ramon et al. 2006](#); [Kaiser 2006](#); [Gupta et al. 2006](#); [Kylafis et al. 2008](#); [Maitra et al. 2009](#); [Pe'er & Casella 2009](#); [Pe'er & Markoff 2012](#); [Markoff et al. 2015](#); [O' Riordan et al.](#)

2016b). Understanding the funnel mass-loading could be crucial for breaking this degeneracy and constraining the role of the jet in producing the observed high-energy X-ray emission in the low/hard state.

For our empty funnel models, we set the plasma density in the funnel to zero. However, this case represents a wider class of models in which the funnel contains material that does not contribute significantly to the emission. For example, models in which the proton-to-electron temperature ratio in the jet is comparable to that in the disk result in similar spectra to the empty funnel cases. This is because the denser funnel wall dominates the jet component unless the plasma in the centre of the funnel is hot enough. For similar assumptions about the electron temperatures, the spectra from more complicated matter profiles in force-free jets should fall within the two extremes considered here. We will investigate observational signatures of the regime where the force-free approximation breaks down (Globus & Levinson 2013) in a future work, which will require significant modifications to our dynamical models.

We have not specified a mass-loading mechanism, but have simply compared spectra from the empty funnel case to the extreme case of a steady, force-free funnel with constant mass and internal energy density profiles. As well as spectral properties, we expect that variability studies will play a key role in constraining the mass-loading physics systems such as Sgr A* and M87. Importantly, many of the proposed mass-loading mechanisms operate on very different time-scales, and so could in principle be distinguished by the EHT. For example, pair production by vacuum gaps in the black hole magnetosphere is expected to be intermittent, and vary on timescales comparable to the light-crossing time of the black hole (Levinson & Rieger 2011; Broderick & Tchekhovskoy 2015). M87 is a promising candidate for studying horizon-scale temporal variability, since the light-crossing time is roughly equal to one day. For Sgr A* this timescale is roughly equal to one minute and so is too short to be directly imaged. However, such short timescales could be probed by analyzing closure quantities (Doeleman et al. 2009b). It is possible that other mass-loading processes may operate on timescales significantly longer than the light-crossing time. For example, pairs may be produced by photon annihilation

(Mościbrodzka et al. 2011) on timescales determined by radiation field of the disk. Furthermore, magnetohydrodynamic processes such as magnetic Rayleigh-Taylor instabilities in the funnel wall (McKinney et al. 2012, and Appendix A), or magnetic field polarity inversions in the disk Dexter et al. (2014) can inject matter from the disk into the centre of the funnel. These processes operate on spatial scales much larger than the Schwarzschild radius, and so the corresponding variability could be resolved by future observations.

A significant limitation of the current work is our simplified treatment of the emitting electrons. In particular, we neglect the contribution from non-thermal electrons which might be present due to acceleration by shock waves (e.g., Sironi et al. 2015), magnetic reconnection (e.g., Sironi & Spitkovsky 2014), or due to the injection process itself (e.g., Levinson & Rieger 2011). Although these non-thermal electrons would likely affect the high-frequency emission in our spectra, including these processes would introduce additional poorly-constrained free parameters into our models, and so we neglect this contribution as a first step. Furthermore, although we allow the proton-to-electron temperature ratio to vary as a function of the plasma β , significant uncertainties remain in the electron thermodynamics of collisionless accretion flows (Ressler et al. 2015; Foucart et al. 2016; Sądowski et al. 2017). Hopefully, these uncertainties will be clarified further by upcoming observations with the EHT.

The authors would like to thank Alexander Tchekhovskoy for providing simulation data. AP and MOR acknowledge the DJEI/DES/SFI/HEA Irish Centre for High-End Computing (ICHEC) for the provision of computational facilities under project ucast008b. MOR is supported by the Irish Research Council under grant number GOIPG/2013/315. This research was partially supported by the European Union Seventh Framework Programme (FP7/2007-2013) under grant agreement no 618499. JCM acknowledges NASA/NSF/TCAN (NNX14AB46G), NSF/XSEDE/TACC (TG-PHY120005), and NASA/Pleiades (SMD-14-5451).

Software: HARM (Gammie et al. 2003), grmonty (Dolence et al. 2009)

APPENDIX

A. MASS AND INTERNAL ENERGY DENSITIES IN MAD AND SANE GRMHD MODELS

In Figure A1 we show (ϕ -averaged) snapshots of our MAD and SANE GRMHD models. The left panels show the mass density, and the right panels show the internal energy density. As in Figure 1, the top panel shows the thin MAD model with $H/R \approx 0.2$ and $a = 0.99$, the middle panel shows the thick MAD model with $H/R \approx 1$ and $a = 0.9375$, and the bottom panel shows the SANE model with $H/R \approx 0.2$ and $a = 0.92$. In these plots, the funnel regions have

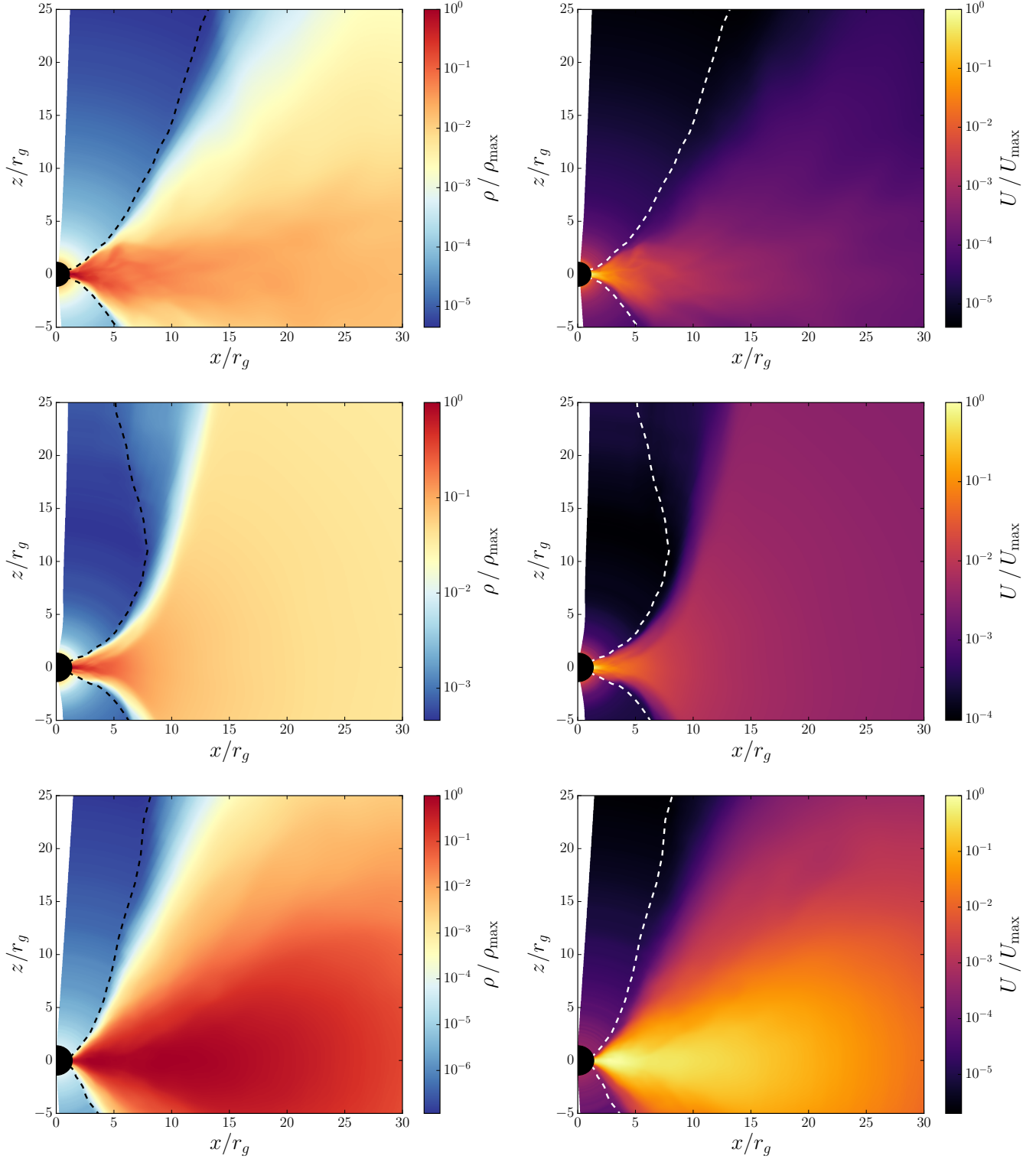


Figure A1. Snapshots of our MAD and SANE GRMHD models. The left panels show the mass density, and the right panels show the internal energy density. The top panel shows the thin MAD model with $H/R \approx 0.2$ and $a = 0.99$. The middle panel shows the thick MAD model with $H/R \approx 1$ and $a = 0.9375$. The bottom panel shows the SANE model with $H/R \approx 0.2$ and $a = 0.92$. The funnel regions are manually filled with constant profiles of mass and internal energy densities, according to the prescription described in Section 2. The dashed lines represent the region which is excised in the “empty” funnel models.

been filled with constant profiles of mass and internal energy according to the prescription described in Section 2. The dashed lines represent the regions affected by the numerical floor material (prior to the manual filling of the funnel), which are excised in the “empty” funnel models. The jet in the thick MAD model (middle panel) has a region near $r \approx 20 r_g$ which is not affected by the numerical density floors. Instead, this is material which has moved from the disk into the funnel due to instabilities at the jet-disk interface (McKinney et al. 2012). This is a transient feature, which has little effect on the spectra in this case. However, such disk-jet instabilities are a possible physical mechanism for mass-loading the jet.

B. DEPENDENCE OF THE SPECTRA ON THE BLACK HOLE MASS AND MASS ACCRETION RATE

The synchrotron luminosity scales with the fluid properties as $L_{\text{syn}} \sim \rho B^2 \Theta^2 V$, where ρ is the mass density, B is the magnetic field strength, $\Theta = kT/mc^2$ is the electron temperature, and V is the volume of the emitting region. The mass density scales with the black hole mass and accretion rate as $\rho \sim \dot{M} t_g / V \sim \dot{M} / M^2$, where we have used that $t_g = r_g / c \sim M$ and $V \sim M^3$. The magnetic energy density scales in the same way. Since we are neglecting radiation pressure, the electron temperature is simply proportional to the ratio of the internal and mass energy densities and so is independent of M and \dot{M} . Therefore, the luminosity scales as $L_{\text{syn}} \sim \dot{M}^2 / M$. It is convenient to write the accretion rate as a fraction η of the Eddington rate \dot{M}_{Edd} . Since \dot{M}_{Edd} is proportional to the black hole mass, we find that $\rho \sim \eta / M$ and so $L_{\text{syn}} \sim \eta^2 M$. We can follow the same procedure to find scalings for the synchrotron frequency $\nu_{\text{syn}} \sim B \Theta^2 \sim \sqrt{\eta / M}$, the optical depth $\tau = n \sigma_T R \sim \eta$, and the Compton y parameter $y = 16 \Theta^2 \tau \sim \eta$ (Rybicki & Lightman 1979). We conclude that the luminosities of the synchrotron and Compton spectral components depend strongly on the mass accretion rate as $L_{\text{syn}} \sim \dot{M}^2$ and $L_{\text{Compton}} = y L_{\text{syn}} \sim \dot{M}^3$, while the frequencies of these components depend only weakly on \dot{M} as $\nu_{\text{syn}} \sim \dot{M}^{1/2}$ and $\nu_{\text{Compton}} \sim \Theta^2 \nu_{\text{syn}} \sim \dot{M}^{1/2}$.

REFERENCES

- Baganoff, F. K., Maeda, Y., Morris, M., & et. al. 2003, *ApJ*, 591, 891
- Ball, D., Özel, F., Psaltis, D., & Chan, C.-k. 2016, *ApJ*, 826, 77
- Blandford, R. D. & Znajek, R. L. 1977, *MNRAS*, 179, 433
- Bosch-Ramon, V., Romero, G. E., & Paredes, J. M. 2006, *A&A*, 447, 263
- Broderick, A. E. & Tchekhovskoy, A. 2015, *ApJ*, 809, 97
- Cadolle Bel, M., Sizon, P., Goldwurm, A., Rodriguez, J., et al. 2006, *A&A*, 446, 591
- Chan, C.-k., Psaltis, D., Özel, F., Medeiros, L., Marrone, D., Sądowski, A., & Narayan, R. 2015a, *ApJ*, 812, 103
- Chan, C.-K., Psaltis, D., Özel, F., Narayan, R., & Sądowski, A. 2015b, *ApJ*, 799, 1
- Dexter, J., McKinney, J. C., Markoff, S., & Tchekhovskoy, A. 2014, *MNRAS*, 440, 2185
- Doeleman, S., Agol, E., Backer, D., Baganoff, F., & et. al. 2009a, in *ArXiv Astrophysics e-prints*, Vol. 2010, astro2010: The Astronomy and Astrophysics Decadal Survey
- Doeleman, S. S., Fish, V. L., Broderick, A. E., Loeb, A., & Rogers, A. E. E. 2009b, *ApJ*, 695, 59
- Doeleman, S. S., Weintroub, J., Rogers, A. E. E., & et. al. 2008, *Nature*, 455, 78
- Dolence, J. C., Gammie, C. F., Mościbrodzka, M., & Leung, P. K. 2009, *ApJS*, 184, 387
- Esin, A. A., McClintock, J. E., Drake, J. J., Garcia, M. R., Haswell, C. A., Hynes, R. I., & Muno, M. P. 2001, *ApJ*, 555, 483
- Esin, A. A., McClintock, J. E., & Narayan, R. 1997, *ApJ*, 489, 865
- Falcke, H., Körtling, E., & Markoff, S. 2004, *A&A*, 414, 895
- Foucart, F., Chandra, M., Gammie, C. F., & Quataert, E. 2016, *MNRAS*, 456, 1332
- Gammie, C. F., McKinney, J. C., & Tóth, G. 2003, *ApJ*, 589, 444
- Gierlinski, M., Zdziarski, A. A., Done, C., Johnson, W. N., Ebisawa, K., Ueda, Y., Haardt, F., & Philips, B. F. 1997, *MNRAS*, 288, 958
- Gillessen, S., Eisenhauer, F., Trippe, S., Alexander, T., Genzel, R., Martins, F., & Ott, T. 2009, *ApJ*, 692, 1075
- Globus, N. & Levinson, A. 2013, *PhRvD*, 88, 084046
- Gold, R., McKinney, J. C., Johnson, M. D., & Doleman, S. S. 2017, *ApJ*, 837, 180
- Gupta, S., Böttcher, M., & Dermer, C. D. 2006, *ApJ*, 644, 409
- Kaiser, C. R. 2006, *MNRAS*, 367, 1083
- Kylafis, N. D., Papadakis, I. E., Reig, P., Giannios, D., & Pooley, G. G. 2008, *A&A*, 489, 481
- Levinson, A. & Rieger, F. 2011, *ApJ*, 730, 123
- Magdziarz, P. & Zdziarski, A. A. 1995, *MNRAS*, 273, 837
- Maitra, D., Markoff, S., Brocksopp, C., Noble, M., Nowak, M., & Wilms, J. 2009, *MNRAS*, 398, 1638
- Markoff, S., Falcke, H., & Fender, R. 2001, *A&A*, 372, L25
- Markoff, S., Nowak, M., Corbel, S., Fender, R., & Falcke, H. 2003, *A&A*, 397, 645
- Markoff, S., Nowak, M. A., Gallo, E., et al. 2015, *ApJL*, 812, L25
- Markoff, S., Nowak, M. A., & Wilms, J. 2005, *ApJ*, 635, 1203
- McKinney, J. C. & Blandford, R. D. 2009, *MNRAS*, 394, L126
- McKinney, J. C. & Gammie, C. F. 2004, *ApJ*, 611, 977
- McKinney, J. C., Tchekhovskoy, A., & Blandford, R. D. 2012, *MNRAS*, 423, 3083
- Mirabel, I. F. & Rodríguez, L. F. 1994, *Nature*, 371, 46
- Mościbrodzka, M. & Falcke, H. 2013, *A&A*, 559, L3
- Mościbrodzka, M., Falcke, H., Shiokawa, H., & Gammie, C. F. 2014, *A&A*, 570, A7
- Mościbrodzka, M., Gammie, C. F., Dolence, J. C., & Shiokawa, H. 2011, *ApJ*, 735, 9
- Mościbrodzka, M., Gammie, C. F., Dolence, J. C., Shiokawa, H., & Leung, P. K. 2009, *ApJ*, 706, 497
- Narayan, R., Igumenshchev, I. V., & Abramowicz, M. A. 2003, *PASJ*, 55, L69
- Narayan, R. & McClintock, J. E. 2008, *NewAR*, 51, 733
- Narayan, R., Sądowski, A., Penna, R. F., & Kulkarni, A. K. 2012, *MNRAS*, 426, 3241
- Neilsen, J., Nowak, M. A., Gammie, C., & et. al. 2013, *ApJ*, 774, 42

- Niedźwiecki, A., Xie, F.-G., & Stępnik, A. 2014, *MNRAS*, 443, 1733
- Niedźwiecki, A., Xie, F.-G., & Zdziarski, A. A. 2012, *MNRAS*, 420, 1195
- O' Riordan, M., Pe'er, A., & McKinney, J. C. 2016a, *ApJ*, 831, 62
- . 2016b, *ApJ*, 819, 95
- Pe'er, A. & Casella, P. 2009, *ApJ*, 699, 1919
- Pe'er, A. & Markoff, S. 2012, *ApJ*, 753, 177
- Poutanen, J. 1998, in *Theory of Black Hole Accretion Disks*, ed. M. A. Abramowicz, G. Bjornsson, & J. E. Pringle (Cambridge University Press), 100–122
- Psaltis, D., Özel, F., Chan, C.-K., & Marrone, D. P. 2015, *ApJ*, 814, 115
- Qiao, E. & Liu, B. F. 2015, *MNRAS*, 448, 1099
- Ressler, S. M., Tchekhovskoy, A., Quataert, E., Chandra, M., & Gammie, C. F. 2015, *MNRAS*, 454, 1848
- Ressler, S. M., Tchekhovskoy, A., Quataert, E., & Gammie, C. F. 2017, *MNRAS*, 467, 3604
- Ryan, B. R., Ressler, S. M., Dolence, J. C., Tchekhovskoy, A., Gammie, C., & Quataert, E. 2017, *ApJL*, 844, L24
- Rybicki, G. B. & Lightman, A. P. 1979, *Radiative Processes in Astrophysics* (New York, Wiley-Interscience)
- Sądowski, A., Wielgus, M., Narayan, R., Abarca, D., McKinney, J. C., & Chael, A. 2017, *MNRAS*, 466, 705
- Shcherbakov, R. V. & McKinney, J. C. 2013, *ApJL*, 774, L22
- Shcherbakov, R. V., Penna, R. F., & McKinney, J. C. 2012, *ApJ*, 755, 133
- Sironi, L., Keshet, U., & Lemoine, M. 2015, *SSRv*, 191, 519
- Sironi, L. & Spitkovsky, A. 2014, *ApJL*, 783, L21
- Tchekhovskoy, A., Narayan, R., & McKinney, J. C. 2010, *ApJ*, 711, 50
- . 2011, *MNRAS*, 418, L79
- Titarchuk, L. 1994, *ApJ*, 434, 570
- Yuan, F., Zdziarski, A. A., Xue, Y., & Wu, X.-B. 2007, *ApJ*, 659, 541